Journal of Materials Chemistry C

TiO2/(BiO)2CO3 Nanocomposites for Ultraviolet Filtration with Reduced Photocatalytic Activity

Journal:	*Journal of Materials Chemistry C*
Manuscript ID	TC-ART-03-2018-001330.R1
Article Type:	Paper
Date Submitted by the Author:	11-May-2018
Complete List of Authors:	Bogusz, Kathrin; University of Wollongong, ISEM Tehei, Moeava; University of Wollongong, School of Chemistry and Centre for Medical Bioscience; Australian Institute of Nuclear Science and Engineering , Lerch, Michael; University of Wollongong, School of Engineering Physics Dou, Shi; University of Wollongong, University of Wollongong, Institute for Superconducting and Electronic Materials Liu, Huakun; University of Wollongong, ISEM Konstantinov, Konstantin; University of Wollongong, Institute for Superconducting and Electronic Materials

$TiO_2/(BiO)_2CO_3$ Nanocomposites for Ultraviolet Filtration with Reduced Photocatalytic Activity

Kathrin Bogusz, [†,‡] Moeava Tehei, [‡,§,ǁ], Michael Lerch, [‡,ǁ], Shi X. Dou, [†] Hua K. Liu, [†] and Konstantin Konstantinov*[,†,‡]

[†] Institute for Superconducting and Electronic Materials, Australian Institute for Innovative Materials, University of Wollongong, NSW 2522, Australia.

[‡]Illawarra Health and Medical Research Institute, University of Wollongong, NSW 2522, Australia.

[§]School of Chemistry, Faculty of Science, Medicine and Health, University of Wollongong, NSW 2522, Australia.

[ǁ]Centre for Medical and Radiation Physics, Faculty of Engineering and Information Science, University of Wollongong, NSW 2522, Australia.

*Email - konstan@uow.edu.au

ABSTRACT

TiO_2 nanoparticles are typically used in sunscreens; however, they have shown to exhibit cyto- and genotoxicity, which is related to the photocatalytic activity and the subsequent formation of reactive oxygen species when exposed to ultraviolet radiation. In this study, we synthesised nanocomposite materials consisting of TiO_2 nanoparticles and homogeneously attached $(BiO)_2CO_3$ clusters with a size < 10 nm onto their surfaces. The nanocomposites were prepared using a facile precipitation approach with different atomic ratios of Bi/Ti of 0.02, 0.04, and 0.08. The TiO_2/$(BiO)_2CO_3$ nanocomposites exhibit an absorbance in the ultraviolet-visible range that is similar to that of TiO_2 nanoparticles and photocatalytic activity that is reduced by up to 60% when exposed to ultraviolet and visible light. In addition, the nanocomposites show high biocompatibility in healthy HaCaT human skin cells and Madin-Darby canine kidney cells *in vitro*, and more importantly, they are capable of reducing the photo-generated toxicity of TiO_2 in HaCaT cells upon irradiation with simulated sunlight. Such multifunctional nanocomposites could potentially be applied as alternative ultraviolet filter components in sunscreen formulations, reducing potential adverse effects associated with TiO_2 nanoparticles.

Keywords: TiO_2, $(BiO)_2CO_3$, nanocomposite, photocatalytic activity, UV protection

1 INTRODUCTION

Inorganic nanoparticles (NPs), such as TiO_2 are commonly used as ultraviolet (UV) filters in sunscreen formulations, which can reduce the effects of harmful solar UV radiation, in particular UVA (320 – 400 nm) and UVB (290 – 320 nm). Not only can UV radiation lead to the formation of skin cancer, it also promotes photo-aging and genetic damage through the generation of reactive oxygen species (ROS).[1, 2] The use of NPs also raises safety concerns, however, due to possible negative side effects of the small-sized particles on the human body, which is a topic of ongoing discussion in the research community.[3, 4] Although the nanometer size is crucial, since it offers improved photoprotection and transparency in the visible range as compared with the bulk materials,[5] some NPs can easily penetrate into the skin and be incorporated into human cells, where TiO_2 NPs have shown to exhibit cyto- and genotoxicity.[6] The toxicity is associated with the photocatalytic activity of the NPs and the subsequent formation of ROS when exposed to UV radiation.[4, 7] Moreover, these reactive species can lead to enhanced degradation of commonly added organic sunscreen components, which typically exhibit lower photostability than the inorganic additives.[8] After application to the skin and exposure to UV-visible radiation, the degradation can result in a decrease in sun protection factor (SPF) or worse, the formation of unknown, toxic intermediates.[9] Approaches to minimize the photocatalytic activity of the active inorganic sunscreen ingredients include the coating of TiO_2 NPs with silica, but complete protection has not been achieved as yet.[6]

Bismuth-based compounds have shown biocompatibility and have already been used in cosmetics and medicine.[10, 11] For instance, BiOCl is used in mineral powder in makeup, and Bi_2O_3 has been used as an astringent.[10, 12] Inorganic bismuth salts are used for the treatment of gastric and duodenal ulcers,[13] and organobismuth compounds have antifungal, antimicrobial, and anticancer activities.[14, 15] $(BiO)_2CO_3$ has been widely investigated as an

ingredient in protective agents for gastrointestinal diseases,[16] as filler in radiopaque catheters,[17] and in pollution prevention, as it shows photocatalytic and antibacterial activity.[18, 19] Moreover, it is well known that the carbonate ion acts as a hydroxyl radical scavenger, reducing the degradation of organic molecules in waste water.[20, 21] $(BiO)_2CO_3$ has a large band gap (2.9 – 3.6 eV), which is tuneable, depending on its morphological properties.[22] Diverse nanostructures of $(BiO)_2CO_3$ have been synthesised, and studied regarding their photocatalytic activity using dyes, such as rhodamine B, methyl orange, and methylene blue.[22-24] Furthermore, various $(BiO)_2CO_3$ superstructures have been synthesised for the efficient removal of nitrogen monoxide (NO).[25-27] $(BiO)_2CO_3$ has been also investigated in combination with other materials to form $BiVO_4/(BiO)_2CO_3$ nanocomposites,[28] and $(BiO)_2CO_3/BiOI$[29] and α-$Bi_2O_3/(BiO)_2CO_3$[30] heterojunctions as efficient photocatalysts for the removal of toxic pollutants. Recently, a graphene and TiO_2 co-modified $(BiO)_2CO_3$ heterojunction composite was developed through a two-step hydrothermal process that displayed higher photocatalytic activity than the individual compounds.[31] It has to be noted that the photocatalytic activity of $(BiO)_2CO_3$ was reported for a large concentration of the active material, 1 g/L.[23, 24] The study of low concentrations in the mg/L range would therefore be of interest, especially since the great advantage of the $(BiO)_2CO_3$ composite materials lies in the facile synthesis approach, which can include a template-free or hydrothermal process.[32, 33]

In this study, we investigate both the UV blocking potential and the photocatalytic activity of $TiO_2/(BiO)_2CO_3$ nanocomposites, which were prepared using a facile, template-free precipitation method with atomic ratios Bi/Ti of 0.02, 0.04, and 0.08 (2 at.%, 4 at.%, and 8 at.%, respectively). The photocatalytic activity of the $TiO_2/(BiO)_2CO_3$ nanocomposites and pristine TiO_2 NPs was investigated through monitoring crystal violet degradation under UVA/UVB irradiation and simulated solar irradiation (air mass (AM) 1.5 G, 1 sun

equivalent). The cytotoxicity of the $TiO_2/(BiO)_2CO_3$ nanocomposites and pristine TiO_2 NPs was determined in healthy HaCaT and Madin-Darby Canine Kidney (MDCK) cells using the 3-(4,5-dimethylthiazol-2-yl)-2,5-diphenyltetrazolium bromide (MTT) assay at a concentration ranging from 5 – 500 μg/mL and an exposure time of 24 h.

2 MATERIALS AND EXPERIMENTAL METHODS

2.1 Reagents and Materials

All chemicals were analytical grade from commercial sources. TiO_2 (Aeroxide® P25), $Bi(NO_3)_3{\cdot}5H_2O$, 30% NH_4OH, tris(4-(dimethylamino)phenyl)methylium chloride (crystal violet), and ethanol were purchased from Sigma-Aldrich. Aeroxide® P25 is a mixture of anatase and rutile TiO_2 and is often used in commercial sunscreens.[34, 35] 69% HNO_3 was obtained from Merck.

Cellular experiments were carried out with HaCaT and MDCK cells, which were purchased from the European Collection of Cell Cultures (ECACC). Dulbecco's Modified Eagle Medium (DMEM), fetal bovine serum (FBS), penicillin, streptomycin, trypsin ethylenediaminetetraacetic acid (trypsin–EDTA), and phosphate buffered saline (PBS) were purchased from Life Technologies. The MTT dye and dimethyl sulfoxide (DMSO) were purchased from Sigma-Aldrich.

2.2 Preparation of $TiO_2/(BiO)_2CO_3$ Nanocomposites

The $TiO_2/(BiO)_2CO_3$ nanocomposites were synthesised via a two-step precipitation-based method. First, 600 mg of TiO_2 NPs were suspended in 110 mL of deionized (DI) water and sonicated using a sonication bath (Branson 3800, Ultrasonics Corp) for 1 h. Then, according to the atomic ratio of Bi/Ti, $Bi(NO_3)_3{\cdot}5H_2O$ was dissolved in 0.75 – 2.95 mL of 69% HNO_3.

The acid was 50% neutralized with the dropwise addition of 30% NH_4OH. Then, the reaction mixture was added to the suspension of TiO_2 and stirred for 2 min. Further NH_4OH was added dropwise until the pH reached a value of 8. The precipitates were filtered and washed with deionised (DI) water, suspended in 35 – 50 mL DI water, and heated under stirring at 80 – 100ºC for 5.5 h. Then, the composites were filtered and washed with DI water, and the colourless powder was dried in vacuum at 60ºC for 48 h. The samples were denoted as Bi/Ti 2 at.%, Bi/Ti 4 at.%, and Bi/Ti 8 at.% for the composites with Bi:Ti atomic ratios of 0.02, 0.04, and 0.08, respectively.

2.3 Materials Characterization

The phase of the produced and as-received nanopowders was characterized using an Enhanced Mini-Materials Analyzer (EMMA) X-Ray Diffractometer (XRD; GBC Scientific) with Cu Kα radiation (λ = 1.5418˚ A) at 40 kV and 25 mA.

The morphology and particle size of all materials, as well as the chemical composition, were examined using the JEOL 7500 field emission scanning electron microscope (FESEM) at the Electron Microscopy Centre at the Australian Institute of Intelligent Materials (AIIM). Energy dispersive X-ray spectra (EDS) were obtained using a X-Flash 4010 10 mm^2, 127 eV SDD energy dispersive X-ray detector (Bruker, Massachusetts, USA). High resolution EDS mapping and high resolution transmission electron microscope (TEM) images were obtained using a JEM-ARM200F atomic resolution microscope fitted with a Centrino SDD 100 mm^2 detector (JEOL, Akishima, Tokyo, Japan). The samples were prepared on carbon-coated copper grids, and the crystal size distribution was surveyed using Image-J software.

The Brunauer-Emmet-Teller (BET) specific surface area of all materials was measured using a Nova 1000 high speed gas sorption analyser from Quantachrome. The adsorption of N_2 at

the temperature of liquid nitrogen was determined, and prior to measuring, the samples were degassed at 60 °C for 15 h in vacuum.

The surface composition of the produced and as-received nanopowders was evaluated via X-ray photoelectron spectroscopy (XPS) using a SPECS PHOIBOS 100 Analyzer installed in a high vacuum chamber with the base pressure below 10^{-8} mbar. X-ray excitation was provided by Al Kα radiation with a photon energy of 1486.6 eV at the high voltage of 12 kV and power of 120 W. The XPS binding energy spectra were recorded with the pass energy of 20 eV in the fixed analyser transmission mode. Analysis of the XPS data was carried out using CasaXPS 2.3.15 software.

2.4 UV-Visible Spectroscopy and Photocatalytic Activity

The absorbance was recorded on an UV-3600 spectrophotometer from Shimadzu Corporation (Kyoto, Japan) over the range of 800 to 200 nm using quartz cuvettes. The NP suspensions were prepared in DI water at a concentration of 25 µg/mL. The band gap was determined using Equation (1):[36]

$$(\alpha h\nu)^n = A\left(h\nu - E_g\right) \qquad (1)$$

where α, h, ν, A, and E_g are the absorption coefficient, Planck constant, light frequency, a constant, and the band gap, respectively. The value of n depends on the type of optical transition of a semiconductor (i.e., n = 2 for a direct transition and n = 0.5 for an indirect transition). The band gap can be estimated from a plot of $(\alpha h\nu)^n$ vs. the energy ($h\nu$) and the generation of a tangent to the x-axis.

The photocatalytic activity of all prepared nanomaterials and of the pristine TiO_2 NPs under a broad UVA-UVB spectrum was examined using a RPR-200 photochemical reactor (Rayonet, Branford, CT, USA), equipped with 3000 and 3500 Å lamps. TiO_2 is known to generate •OH radicals upon exposure to UV light.[37] When the radicals are in contact with crystal violet, its

central double bond can be cleaved, which results in a decolourisation of the dye. Thus, the degradation of crystal violet – with an absorbance maximum at 590 nm – can be used as an indicator for the amount of generated •OH radicals. The initial concentration of crystal violet was 12 µmol/L and the amount of suspended TiO_2 NPs and $TiO_2/(BiO)_2CO_3$ nanocomposites was 5 mg/L. Before the irradiation with UV light, the nanomaterial suspension containing the crystal violet dye was equilibrated by stirring in the dark for 60 min. Then, a first aliquot was taken just before the irradiation start and its absorbance was measured after removal of the photocatalyst via centrifugation to determine the initial concentration of the dye. Afterwards, the measured aliquots were resuspended and added back to the reaction mixture. Upon exposure to UV light, aliquots were withdrawn every 5 min for a total of 30 min, and the absorbance was measured. The photocatalytic activity was further examined under simulated solar irradiation for a total time of 6 h, using a halogen lamp (50 watt power) and illumination of AM 1.5 G one sun (100 mW/cm^2). The conditions were the same as for the irradiation with UV light only, and the absorbance was determined after every 30 min of irradiation. The apparent rate constant *k* was calculated according to Equation (2):[38]

$$c = c_0 e^{-kt} \qquad (2)$$

where *c* is the concentration as the reaction progresses, c_0 is the initial concentration, and *t* is the time. The integrated first order rate law is shown in Equation (3):

$$\ln\left(\frac{c}{c_0}\right) = -kt \qquad (3)$$

2.5 Cell Culture

Cellular experiments were carried out with HaCaT and MDCK cells. While HaCaT cells are transformed keratinocytes and are derived from histologically normal adult human skin, MDCK cells are derived from the kidney tubule of a normal female adult Cocker Spaniel. The cell cultures were grown and maintained at 37ºC with 5% (v/v) CO_2 in a T75 cm^2 tissue

culture flask (Falcon) containing DMEM supplemented with L-glutamine, 10% (v/v) FBS, and 1% (v/v) penicillin/streptomycin.

2.6 *In Vitro* Cell Viability Assay

Under absence of simulated sunlight

The viability of human skin (HaCaT) cells and MDCK cells was assessed by the MTT assay as described by Mosmann,[39] which is based on the conversion of water-soluble yellow tetrazolium salt to water-insoluble purple formazan. Since this reduction occurs in the mitochondria of viable cells, the amount of formazan produced is directly proportional to the number of viable cells.[40] Typically, the cells were seeded in a 96-well plate and incubated at 37°C. Suspensions of TiO_2, and $TiO_2/(BiO)_2CO_3$ were prepared in PBS (without Ca^{2+} and Mg^{2+}) at a concentration of 1 mg/mL and sonicated for 2 h using a sonication bath (Branson 3800, Ultrasonics Corp). The NP suspensions were then diluted in growth medium and added to the seeded wells to yield concentrations of 0, 5, 10, 25, 50, 100, 250, and 500 µg/mL. After 24 h of incubation at 37°C, the growth medium was removed from each well and replaced with 100 µL of fresh medium and 10 µL of MTT solution, which was prepared in advance and contains 0.5 mg of MTT dye dissolved in 1 mL of PBS (without Ca^{2+} and Mg^{2+}). The well plate was incubated for 4 h until a purple-coloured formazan product was formed. After 85 µL of the test solution was removed, 100 µL of DMSO was added to the wells to dissolve the formazan crystals. The well plate was incubated for 10 min at 37°C and centrifuged at 1200 rpm for 5 min to settle the remaining NPs. Then, 100 µL of supernatant was transferred to a new well of a 96-well plate and the absorbance was measured at a wavelength of 540 nm using a microplate reader (SpectraMax 384 Plaus (Molecular Devices)). The absorbance of the treated wells was compared to the control wells, and the cell viability was expressed as

relative percentage. The MTT assay was performed independently in triplicate for each nanomaterial.

Under presence of simulated sunlight

To ensure that the nanomaterials develop sufficient photocatalytic activity, TiO_2 NPs were suspended in DPBS (with Ca^{2+} and Mg^{2+}, 1 mg/mL), sonicated for 2 h, and added to a solution of crystal violet in DPBS in a 96-well plate at concentrations of 25, 50, and 100 µg/mL. After a dark adsorption of 60 min, the absorbance was measured at 590 nm. The 96-well plate was then placed without the lid on an ice block underneath the light source (300 W Sunlamp, Ultra-Vitalux®, OSRAM), which was pre-run for 30 min to ensure stabilization of the output. The light emission profile of the lamp is shown in Figure S1 in the Supporting Information. The light intensity was measured using a calibrated UVA/B light meter (model 850009, Sper Scientific) and was found to be 6 mW/cm^2 at the surface of the wells. The 96-well plate was irradiated for 15 min, which equals a dose of 5.4 J/cm^2. Afterwards, the absorbance was measured and the amount of degraded crystal violet was determined.

HaCaT cells were seeded in 96-well plates and suspensions of TiO_2 and $TiO_2/(BiO)_2CO_3$ (Bi/Ti 8 at.%) were prepared as described above. Prior to the addition of the NP suspension to the cells the growth medium was replaced with 100 µL of DPBS. The NP suspensions were then added to the cells to yield concentrations of 25, 50, and 100 µg/mL. This concentration range was chosen to ensure the observation of detectable photocatalytic effects while keeping the toxicity related to the nanomaterials to a minimum. The control cells were treated with the equivalent amount of PBS. The cells were incubated with the nanomaterials for 45 min at 37°C. The culture plate lid was then removed and the 96-well plate was placed on an ice block underneath the light source. The cells were irradiated under the same conditions as described above (for 15 min with simulated sunlight and a light intensity of 6 mW/cm^2).

After irradiation, DPBS was replaced with 100 µL of supplemented growth medium and the 96-well plate was incubated for 24 h before fresh medium and MTT dye were added, and the absorbance was measured, as described above.

3 RESULTS AND DISCUSSION

3.1 Identification, Size, Morphology, and Surface Composition of $TiO_2/(BiO)_2CO_3$ Nanocomposites

Figure 1 displays the XRD patterns of the commercial TiO_2 NPs and the synthesised nanomaterials, which can be identified as nanocomposites of the type $TiO_2/(BiO)_2CO_3$. The XRD pattern of the TiO_2 NPs shows reflections attributed to the anatase (JCPDS 01-075-2552) and rutile (JCPDS 01-075-1753) phases. The nanocomposites do not alter the diffraction patterns of the core materials, but lead to additional reflections in the XRD pattern which are assigned to $(BiO)_2CO_3$ (JCPDS 00-41-1488). Moreover, the relative intensity of the reflections increases with increased bismuth present in the nanocomposite.

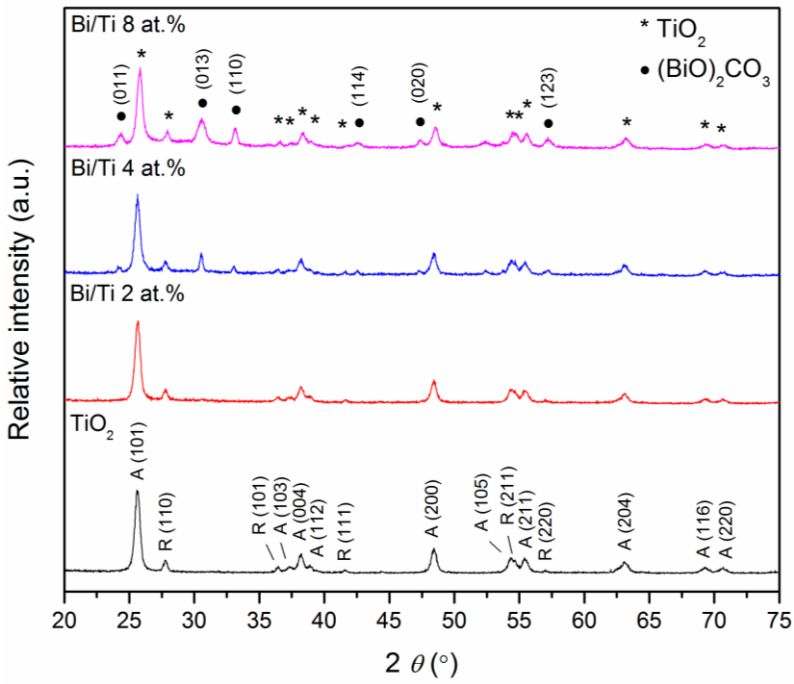

Figure 1. XRD patterns of commercial TiO_2 NPs, and the $TiO_2/(BiO)_2CO_3$ nanocomposites Bi/Ti 2, 4, and 8 at.%.

Typically, the synthesis of $(BiO)_2CO_3$ requires the use of templates or hydrothermal treatments. In this work, however, the TiO_2 NPs act as primary nucleation centres during the nanocomposite synthesis. It was shown that TiO_2 NPs can act as substrate seeds on which a single spherical domain of inverse spinel iron oxide can be epitaxially grown.[41] The seeds can act as efficient catalysts and provide a lower energy barrier for heterogeneous nucleation, in comparison to homogeneous nucleation.[42] The two-step precipitation method used in this work includes the addition of excess ammonium hydroxide, which was used as the precipitating agent, yielding $(BiO)_2CO_3$. It has been shown that the concentration of precipitating agent has a significant influence on the physical properties of $(BiO)_2CO_3$ NPs.[43] Since no carbon source was added to the reaction mixture, the carbonate formation occurred due to the presence of aqueous CO_2. In aqueous solution, carbonic acid, carbon dioxide, bicarbonate, and carbonate exist together in a dynamic equilibrium, as shown in Equations (4) – (6):[44]

$$H_2CO_3(aq) \rightleftharpoons CO_2(aq) + H_2O(l) \quad (4)$$

$$H_2CO_3(aq) \rightleftharpoons H^+(aq) + HCO_3^-(aq) \quad (5)$$

$$HCO_3^-(aq) \rightleftharpoons H^+(aq) + CO_3^{2-}(aq) \quad (6)$$

In acidic environments, the equilibrium shifts to CO_2 (aq), while the addition of a base can shift the equilibrium to the carbonate. In our work, we precipitated the $(BiO)_2CO_3$ clusters using a very slow and dropwise addition of 30% NH_4OH, increasing the pH value gradually. The reaction was complete at a pH of 8 – 9. These principles of carbonate equilibrium chemistry were already used to monitor the rate of inorganic carbon uptake by a variety of algal species.[45]

The BET specific surface area of all materials was measured and is displayed in Table 1. TiO_2 NPs typically show a high specific surface area close to 50 m^2/g.[46] The nanocomposites

display a small decrease in surface area, associated with the coverage of the TiO_2 surface by the $(BiO)_2CO_3$ clusters, due to the increase in the overall size of the NPs.

Table 1. BET Surface Areas and Band Gaps of $TiO_2/(BiO)_2CO_3$ Nanocomposites[a]

Sample	BET surface area (m^2/g)	Band gap (eV)
TiO_2	47.8 ± 0.5	2.68 ± 0.08
Bi/Ti 2 at.%	47.2 ± 0.5	2.83 ± 0.09
Bi/Ti 4 at.%	45.5 ± 0.5	2.79 ± 0.07
Bi/Ti 8 at.%	43.6 ± 0.4	2.69 ± 0.05

[a]Data provided for the pure TiO_2 NPs, and the $TiO_2/(BiO)_2CO_3$ nanocomposites with different Bi/Ti atomic ratios. The indicated errors are the standard deviation.

Figure 2 shows SEM and STEM images of the pure TiO_2 NPs, and the $TiO_2/(BiO)_2CO_3$ nanocomposites with Bi/Ti atomic ratios of 0.02, 0.04, and 0.08. The commercial TiO_2 is made up of mostly rectangular, spherical, ellipsoidal, and prism-like particles with an average particle size of 23.39 ± 8.59 nm (Figure 2a, left image). Figure 2a shows the SEM images of the nanocomposite with Bi/Ti atomic ratios of 0.02, 0.04, and 0.08. For all nanocomposites, the SEM analysis does not show any significant difference in morphology to uncoated TiO_2. The STEM images of the $TiO_2/(BiO)_2CO_3$ composites clearly show that the surfaces of the TiO_2 NPs are covered with very small (< 10 nm) $(BiO)_2CO_3$ clusters (Figure 2b). The coverage with the $(BiO)_2CO_3$ clusters is homogeneous and increases with added $(BiO)_2CO_3$. The HAADF image of the nanocomposite with Bi/Ti 8 at.% (Figure 2b, right image) reveals the interface between TiO_2 and $(BiO)_2CO_3$ clusters and shows rutile TiO_2 with interplanar spacings of 0.30 and 0.33 nm, which is in accordance with the d-spacings of (001) and (110) planes, respectively.

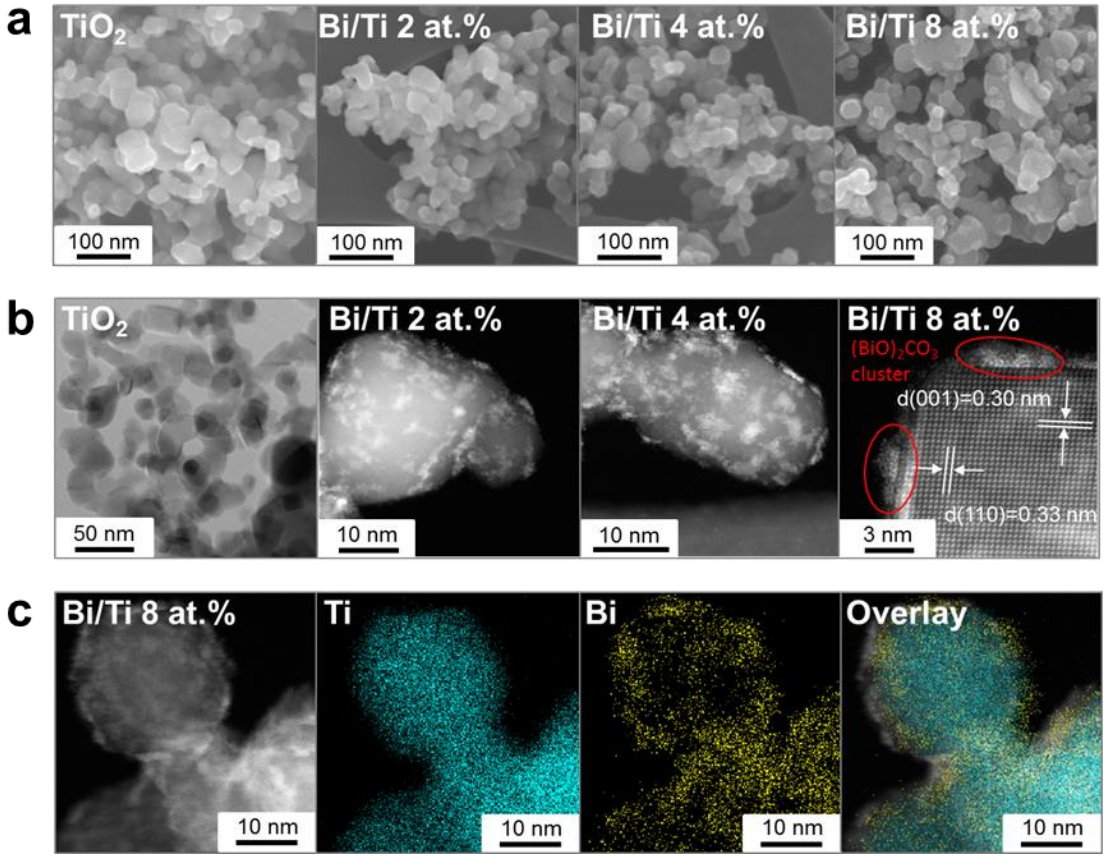

Figure 2. a) SEM images of TiO_2 NPs (left), and the $TiO_2/(BiO)_2CO_3$ nanocomposites with different Bi/Ti atomic ratios. b) HAADF STEM images of TiO_2 NPs (left), the $TiO_2/(BiO)_2CO_3$ nanocomposites with different Bi/Ti atomic ratios. The HAADF image of the nanocomposite with Bi/Ti 8 at.% (right) exposes lattice fringes spaces of 0.30 and 0.33 nm, corresponding to (001) and (110) planes of rutile TiO_2, respectively. c) TEM images with high resolution EDS mapping of the $TiO_2/(BiO)_2CO_3$ nanocomposite Bi/Ti 8 at.%.

The high resolution EDS mapping indicates that the uncoated TiO_2 NPs feature no Bi (Figure S2), while a significant proportion of Bi can be found on the surfaces of the particles for the $TiO_2/(BiO)_2CO_3$ nanocomposites (Figure 2d). The EDS maps of the nanocomposites with Bi/Ti 2 and 4 at.% also displayed a homogeneous distribution of the Bi on the surfaces of the TiO_2 particles, as shown in Figure S2. Uncovered TiO_2 NPs were not found anywhere in the imaged specimens, even for the composite with the smallest amount of $(BiO)_2CO_3$ (Bi/Ti 2 at.%). The Bi/Ti ratio of each of the composites was measured from EDS measurements. The

obtained ratio for the 2, 4 and 8 at.% nanocomposites was 1.73 ± 0.1, 3.76 ± 0.1, and 8.11 ± 0.25 at.%, respectively.

The surface composition of the nanocomposites was characterized using high resolution XPS. Figure 3 displays the high resolution XPS spectra of the Bi 4f orbitals (left column) and the C 1s orbital (right column), and the peak deconvolution results for the pure TiO_2, and TiO_2/$(BiO)_2CO_3$ nanocomposites. While the TiO_2 NPs do not display any Bi 4f orbitals, the presence of $(BiO)_2CO_3$ clusters in Bi/Ti 2 at.% yields a significant signal of the two symmetric Bi 4f peaks with a binding energy of 159 eV (Bi $4f_{7/2}$) and 164 eV (Bi $4f_{5/2}$), which indicates the presence of Bi–O bonds with bismuth in the +3 oxidation state, as found in $(BiO)_2CO_3$.[32, 47] The intensity of the Bi 4f peak increases with increasing atomic ratio of Bi/Ti in the nanocomposite materials. Two Gaussian peaks were used to fit the experimental data in the high resolution XPS spectra of C 1s (right column). The peak at the lower binding energy of 284.83 eV can be assigned to C–C bonds in adventitious carbon.[32] The second C 1s peak at 287 eV is ascribed to the C–O bonds that are usually present in CO_3^{2-}, as found in $(BiO)_2CO_3$.[32] Similarly to the Bi 4f peak, the carbonate-related peak increases in intensity with increasing amounts of $(BiO)_2CO_3$ on the surface of TiO_2. The carbon element in pure TiO_2 corresponds mainly to adventitious hydrocarbon and is not related to the presence of $(BiO)_2CO_3$. All XPS data, including the Ti 2p and O 1s orbitals are summarized in Table S1. The XPS analysis supports the findings from the XRD and TEM analysis and confirms the presence of $(BiO)_2CO_3$ in the nanocomposite materials. The XPS spectra for N 1s, O 1s and Ti 2p are shown in Figure S3. There were no peaks detected in the N 1s area, which excludes the presence of bismuth oxynitrates.[48]

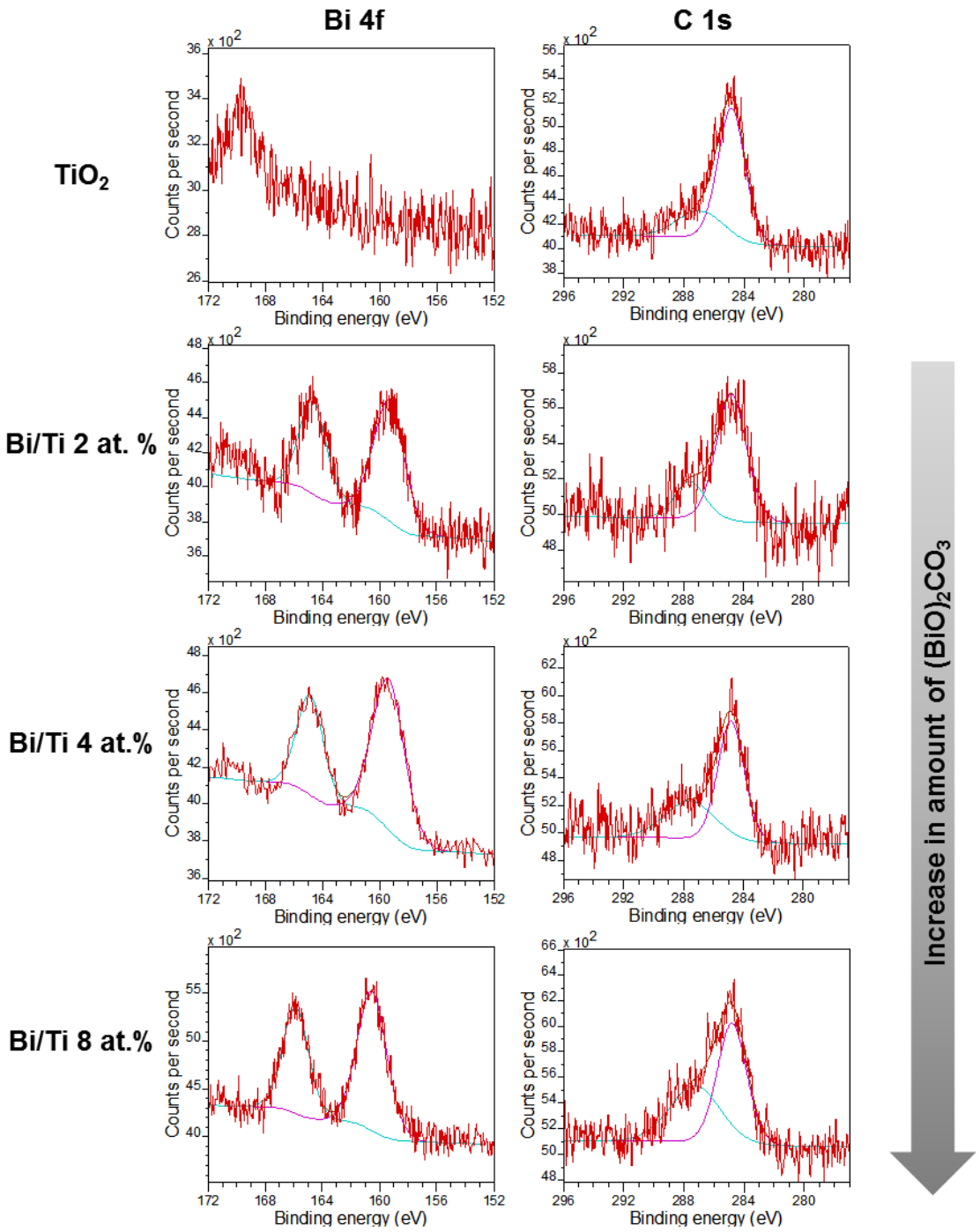

Figure 3. High resolution XPS spectra of the Bi 4f (left column) and C 1s (right column) regions of the commercial TiO_2 NPs, and $TiO_2/(BiO)_2CO_3$ nanocomposites with different Bi/Ti atomic ratios.

3.2 Optical Properties and Band Gap of the $TiO_2/(BiO)_2CO_3$ Nanocomposites

The UV-visible absorption spectrum of each investigated material was measured in order to determine its UV filtering properties and the effects of the $(BiO)_2CO_3$ formed onto the TiO_2 surface on the optical band gap (Figure 4). TiO_2 NPs are a common additive to commercial sunscreen formulations with a high and selective absorbance within the UV region (Figure 4a). The $TiO_2/(BiO)_2CO_3$ nanocomposites exhibit a very similar absorption over the entire UV range as compared to uncoated TiO_2 NPs, with only slightly reduced intensities, depending on the amount of $(BiO)_2CO_3$ clusters present. The reduced absorbance in the visible range is related to the presence of more transparent $(BiO)_2CO_3$ in comparison to TiO_2, which is of advantage in regard to potential application in sunscreen formulations.[22] Moreover, there is only a very small blue shift identified for all tested nanomaterials. These findings suggest that the $(BiO)_2CO_3$ clusters have a negligible impact on the optical properties of the heterojunctions. This is most accurately reflected in a minor increase in the optical band gap of the nanocomposite materials, ranging from 2.69 – 2.83 eV compared to the TiO_2 NPs with an optical band gap of 2.68 ± 0.08 eV, as seen in Table 1. The band gaps of all the materials were calculated using Equation (1) and represent indirect band transitions. The Tauc plots are shown in Figure 4b.

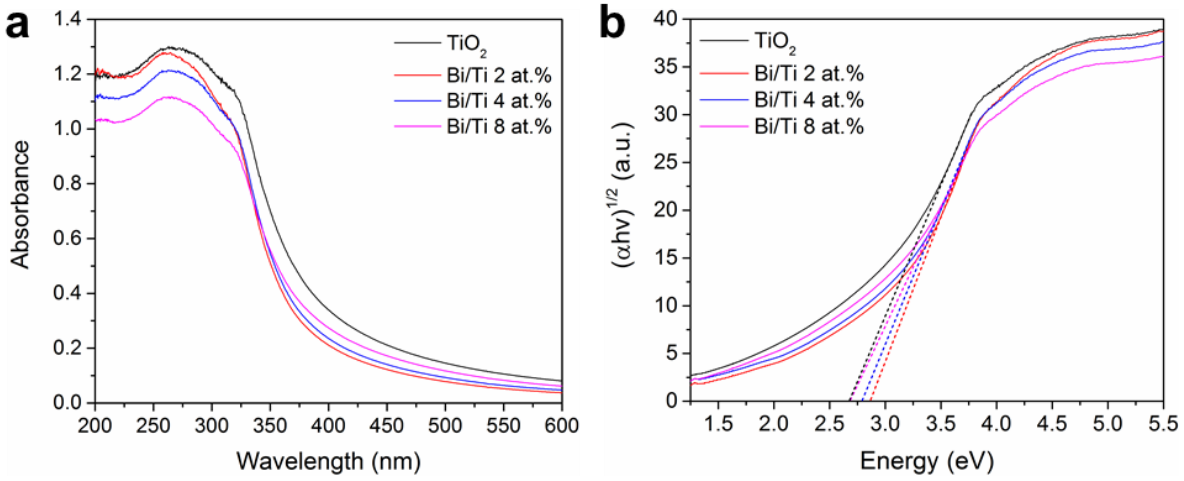

Figure 4. a) UV-visible absorption spectra and b) Tauc plots of pure TiO_2 NPs, and $TiO_2/(BiO)_2CO_3$ nanocomposites with different Bi/Ti atomic ratios. The absorption spectra were recorded at a concentration of NPs of 25 µg/mL in DI water.

3.3 Photocatalytic Activity of the $TiO_2/(BiO)_2CO_3$ Nanocomposites

Each of the nanocomposite materials and the pure TiO_2 NPs were tested for their photocatalytic activity within a broad UVA/UVB spectrum and under simulated solar light irradiation. Crystal violet was utilized as an indicator of the photocatalytic activity and the associated production of hydroxyl radicals. The discoloration of crystal violet in the absence of any photocatalyst was negligible, both under UV and under solar light irradiation. Upon addition to the crystal violet solution of a suspension of TiO_2 at a final concentration of 5 mg/L, the reaction mixture degraded almost completely due to photocatalytic reactions when exposed to UVA and UVB light for 30 min, as shown in Figure 5a. The photocatalytic activity of TiO_2 is generally linked to the particular phase: while anatase TiO_2 exhibits strong photocatalytic activity, the rutile phase is less active.[34, 35] Here, commercial Aeroxide® P25 was used, which is a combination of both anatase and rutile TiO_2. The addition of 5 mg/L of the nanocomposite materials resulted in a significant decrease in degradation of crystal violet in comparison to the pure TiO_2, suggesting a reduction in photocatalytic activity. Furthermore, the reduction in the degradation of crystal violet increased with increasing amounts of $(BiO)_2CO_3$ clusters on the surface of TiO_2. More interestingly, there is only a small difference in degradation between the nanocomposites, which indicates that a coating with $(BiO)_2CO_3$ that results in a Bi/Ti atomic ratio of 0.02, leads to a significant reduction in the photocatalytic activity of the TiO_2 NPs, without affecting the UV blocking properties of TiO_2. The apparent rate constant *k* for each of the materials was calculated using the Langmuir-Hinshelwood model and is shown in Table 2, whereas the plots are displayed in Figures S4 and S5.[49]

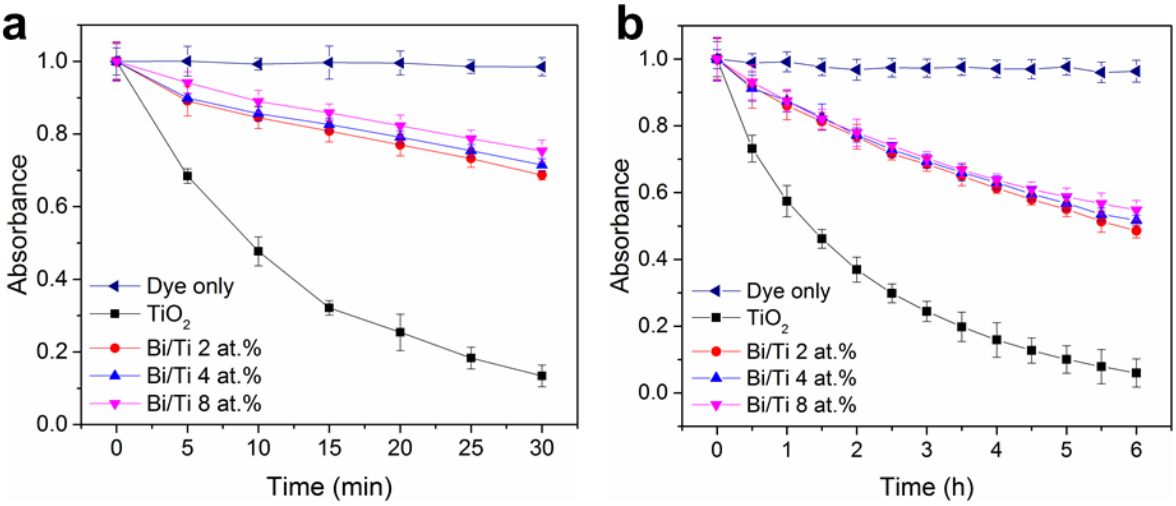

Figure 5. Relative decrease in absorbance of crystal violet solutions containing TiO_2, and $TiO_2/(BiO)_2CO_3$ nanocomposites with different Bi/Ti atomic ratios: a) under UV light exposure, and b) under exposure of AM 1.5 G one sun (100 mW/cm^2). The concentration of all materials is 5 mg/L. The data represent the mean of three independently prepared samples, which were measured separately.

Table 2. Influence of $TiO_2/(BiO)_2CO_3$ Nanocomposites on the Degradation of Crystal Violet[a]

Sample	$k \times 10^{-2}$ (min^{-1}), UV irradiation	$k \times 10^{-2}$ (min^{-1}), sunlight irradiation
Dye only	0.02 ± 0.01	0.47 ± 0.10
TiO_2	6.64 ± 0.22	44.81 ± 0.82
Bi/Ti 2 at.%	1.15 ± 0.04	11.43 ± 0.18
Bi/Ti 4 at.%	1.03 ± 0.04	10.57 ± 0.18
Bi/Ti 8 at.%	0.92 ± 0.03	9.93 ± 0.3

[a]Apparent rate constant *k* for the degradation of crystal violet solutions containing TiO_2, and $TiO_2/(BiO)_2CO_3$ nanocomposites under irradiation by UV light and AM 1.5 G one sun (100 mW/cm^2). The concentration of all materials is 5 mg/L. The errors indicated are the standard deviation obtained through the linear regression.

As displayed in Figure 5b, the degradation of crystal violet under simulated solar light irradiation showed a similar trend to that under UV light in the same system, for an exposure time of 6 h. TiO_2 displays close to 100% degradation after 6 h of simulated solar light irradiation. The apparent rate constants for the nanocomposite materials are 3.9 – 4.5 times smaller than for the pure TiO_2, further confirming the photodegradation protection provided by $(BiO)_2CO_3$ at small concentrations.

The decrease in photocatalytic activity can be attributed to a number of factors, such as a decrease in the BET specific surface area, although the coating with $(BiO)_2CO_3$ in Bi/Ti 2 at.% leads to a decrease in the BET specific surface area of less than 1.5% in comparison to TiO_2. Yet, the photocatalytic activity of that nanocomposite is reduced by over 55% compared to TiO_2. Furthermore, the $(BiO)_2CO_3$ clusters, which are located on the surface of TiO_2, can absorb incoming UV light, reducing the overall radiation that reaches TiO_2. It is shown, however, that even the very small addition of $(BiO)_2CO_3$ to TiO_2 which results in Bi/Ti 2 at.% is sufficient to cause a significant decrease in the degradation of crystal violet. Further addition beyond Bi/Ti 2 at.% has a negligible effect. Therefore, the reduction in photocatalytic activity does not appear to be related to a decrease in the surface area or increased absorption of UV radiation by the $(BiO)_2CO_3$ clusters.

Another explanation for the observed reduced dye degradation can be the very small size of the $(BiO)_2CO_3$ clusters (< 10 nm), which leads to their very high surface/volume ratio. Due to the low crystallinity, the surface is enriched with defects, which can act as ROS scavengers, as shown for CeO_2 NPs.[50, 51] More importantly, it is widely known that carbonate acts as a hydroxyl radical scavenger. Once the carbonate is in contact with hydroxyl radicals, the formation of carbonate radicals is observed, as shown in Equation (7):[52, 53]

$$\bullet OH + CO_3^{2-} \longrightarrow OH^- + CO_3^{-\bullet} \qquad (7)$$

In contrast to hydroxyl radicals, which react rapidly with organic compounds, the carbonate radical is very selective and prolongs the degradation processes, as typically observed in the purification of waste water.[20, 21]

Typically, nanomaterials are designed that increase the photocatalytic activity with the goal of improving the catalyst efficiency.[54, 55] Although the use of $(BiO)_2CO_3$ NPs for photocatalytic purposes is widely reported, $(BiO)_2CO_3$ can also be used as a photoprotector, reducing the photocatalytic activity of the strong photocatalyst TiO_2. $(BiO)_2CO_3$ is a weak photocatalyst on its own, especially at low concentrations such as those used in this work. Noticeable photocatalytic degradation of rhodamine B[23] and methyl orange[24] under UV-visible light irradiation was achieved at concentrations of 1.0 and 0.1 g/L, respectively. The application of $(BiO)_2CO_3$ clusters as a photoprotector is of interest and importance, since TiO_2 NPs are widely used as the active component in sunscreen formulations, although it is known that they generate free radicals.[4, 34]

3.4 *In Vitro* Cell Viability

Under absence of simulated sunlight

The cytotoxicity of the commercial TiO_2 NPs, and the $TiO_2/(BiO)_2CO_3$ nanocomposite materials was determined using the MTT assay, which is based on the conversion of MTT into formazan crystals by viable cells.[40] Non-malignant HaCaT human skin cells and kidney (MDCK) cells were chosen and exposed to the NPs for 24 h at concentrations ranging from 5 – 500 µg/mL (Figure 6). HaCaT keratinocytes are typically used to investigate possible adverse effects of NPs in sunscreens,[56] MDCK cells are used to examine the biocompatibility of NPs, since the kidney represents a possible detoxification route.[57, 58] In general, the reduction of cell viability was observed in a dose-dependent manner for all tested nanomaterials. In both cell lines, the pristine TiO_2 NPs displayed the highest cytotoxicity of

all the tested materials. Nevertheless, at the highest tested concentration of 500 µg/mL, the decrease in mitochondrial activity is still moderate for the TiO_2 NPs, with cell viability of 71.2 ± 4.5% and 61.5 ± 6.6% in HaCaT and MDCK cells, respectively. The $TiO_2/(BiO)_2CO_3$ nanocomposites show cell viabilities that lie above that for the TiO_2 NPs. In addition, the biocompatibility of the nanocomposites increases with increasing atomic ratio of Bi/Ti.

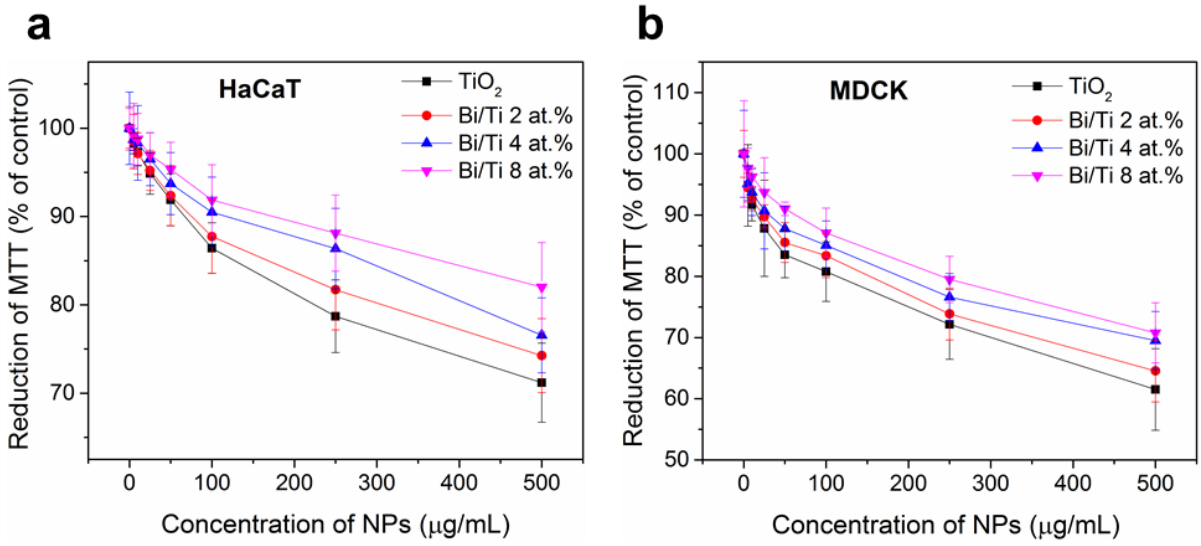

Figure 6. Effects of the commercial TiO_2 NPs, and $TiO_2/(BiO)_2CO_3$ nanocomposites with different Bi/Ti atomic ratios on the mitochondrial function in non-cancerous a) HaCaT human skin cells and b) dog kidney (MDCK) cells. The cells were treated with the NPs at concentrations of 0 (control), 5, 10, 25, 50, 100, 250, and 500 µg/mL for 24 h. At the end of exposure, the mitochondrial function was determined using the MTT reduction assay. The data are represented as the mean of three independently prepared experiments.

Under presence of simulated sunlight

To confirm that the toxicity of TiO_2 is reduced by the inhibition of photocatalytic activity due to $(BiO)_2CO_3$, cell viability assays with HaCaT have been performed under presence of TiO_2, $TiO_2/(BiO)_2CO_3$ (Bi/Ti 8 at.%), and simulated sunlight. To ensure that the chosen concentrations of tested nanomaterials are sufficient to induce detectable photocatalytic

effects, the degradation of crystal violet was evaluated in presence of TiO_2 NPs at 25, 50, and 100 µg/mL and simulated sunlight for 15 min (Figure 7a). A concentration of 25 µg/mL has been shown to be sufficient to cause a degradation of crystal violet of over 33%.

The HaCaT cell viability following exposure to TiO_2 or $TiO_2/(BiO)_2CO_3$ (Bi/Ti 8 a.%) NPs at concentrations of 25, 50, and 100 µg/mL with and without additional simulated sunlight irradiation is shown in Figure 7b. When compared to the toxicity of the nanomaterials alone (non-irradiated), it is clearly visible that the additional exposure to simulated sunlight initiates processes that cause a higher toxicity in HaCaT cells. For instance, at a concentration of 100 µg/mL, the cell viability after treatment with only TiO_2 is high with a survival of 86.4 ± 2.9%, while after additional irradiation with simulated sunlight the cell viability decreases to 64.1 ± 4.4%. This increase in cell mortality is most likely related to the photocatalytic activity of TiO_2 and the subsequent generation of ROS, while the composite is capable of inhibiting a significant amount of photocatalysis.[59, 60] In particular, for the same conditions, the treatment with $TiO_2/(BiO)_2CO_3$ results in a cell viability of 74.5 ± 4.7% after irradiation with simulated sunlight. More interestingly, it is further shown that a significant effect of photocatalysis can only be observed at concentrations ≥ 50 µg/mL, which implies that the impact of photocatalytic activity of TiO_2 on the viability of HaCaT cells is negligible at concentrations ≤ 25 µg/mL.

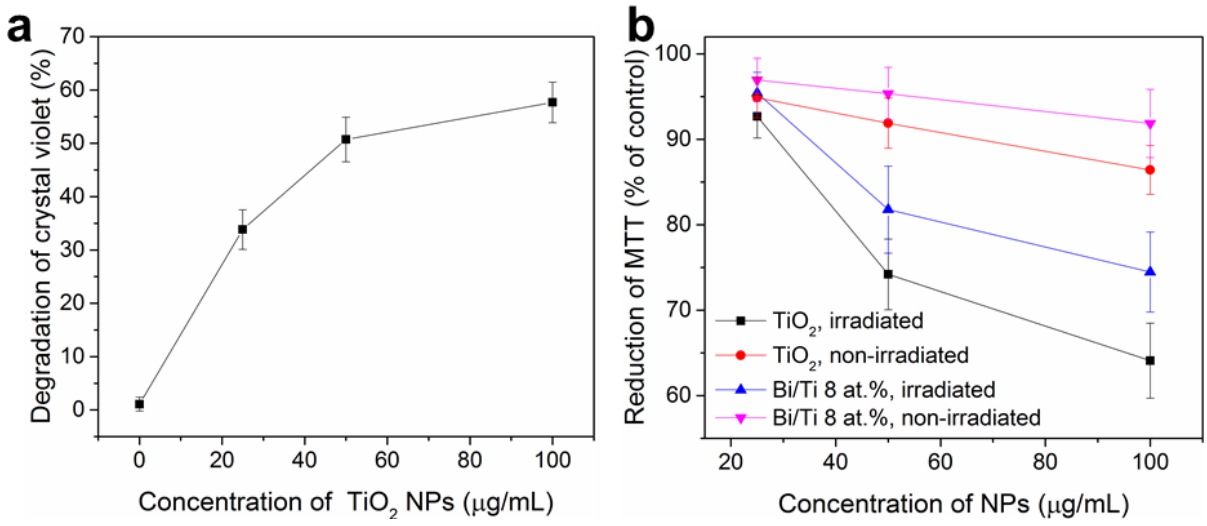

Figure 7. (a) Degradation of crystal violet solutions containing TiO_2 NPs at concentrations of 25, 50, and 100 μg/mL upon irradiation with simulated sunlight for 15 min. (b) Viability of HaCaT cells following exposure to TiO_2 or $TiO_2/(BiO)_2CO_3$ (Bi/Ti 8 a.%) NPs with and without additional simulated sunlight irradiation for 15 min. The viability was assessed using the MTT assay and the tested concentrations were 25, 50, and 100 μg/mL. The data are expressed as percentage of viable cells compared to control cells that have not been exposed to nanomaterials.

The decrease of cell viability of human skin fibroblasts upon exposure to TiO_2 NPs and UV light has been reported widely.[59-61] For instance, the use of rutile TiO_2 and anatase TiO_2 at concentrations of 50 and 100 μg/mL was assessed in HaCaT cells under UVA irradiation with doses of 0 – 10 J/cm^2.[59] No significant toxicity was found towards HaCaT cells exposed to TiO_2 at a concentration of 100 μg/mL without irradiation. Upon irradiation with UVA, however, the anatase TiO_2 treatment resulted in a decrease in cell viability of over 40% at the highest tested dose of 10 J/cm^2, while rutile TiO_2 displayed phototoxicity of less than 20%.[59] Interestingly, the use of a mixture of anatase and rutile (P25), similarly to our work, showed a decrease in cell viability of over 80 and 85% for a dose of 5.4 and 10 J/cm^2, respectively. Although our results show higher cell viability at a dose of 5.4 J/cm^2, the observed trend

highlights the need of more research into the reduction of photocatalytic activity of TiO_2, in particular P25, which is still widely applied in commercial sunscreen formulations.[34, 35] The phototoxicity is generally linked to the generation of ROS in presence of UVA.[59, 60] In particular, an increase in accumulation of intracellular ROS levels by 1.8-fold has been observed in HaCaT cells after 24 h exposure to 200 µg/mL of P25 and irradiation with UVA (365 nm).[60]

As of now, bismuth oxychloride (BiOCl) is the only bismuth-based compound that has been studied in HaCaT cells, although without the application of UVA and UVB light, and simulated sunlight.[62] To the best of our knowledge, neither the toxicity of $(BiO)_2CO_3$ in HaCaT cells, nor the inhibition of photo-induced toxicity of TiO_2 due to the presence of $(BiO)_2CO_3$ upon irradiation with simulated sunlight has yet been reported, which ultimately highlights the novelty of the presented work.

4 CONCLUSION

The commonly used TiO_2 NP additives in sunscreen formulations pose a potential health risk in regard to their ability to generate free radical species that, in turn, can cause cyto- and genotoxicity, either directly through penetration into deep skin tissue or indirectly through the degradation of organic sunscreen additives. The latter case could result in the formation of intermediates with unknown toxicity, which – besides the reduction of SPF – can cause adverse side effects. By reducing the photocatalytic activity of TiO_2 NPs and simultaneously maintaining the UV filtering properties, the health risk of these sunscreen additives can be minimized. Using a simple two-step precipitation approach, we synthesised $TiO_2/(BiO)_2CO_3$ nanocomposites with different atomic ratios of Bi/Ti (0.02, 0.04 and 0.08). The $(BiO)_2CO_3$ clusters are smaller than 10 nm and are evenly distributed throughout the surfaces of the TiO_2 NPs. We demonstrate that, by introducing a small amount of $(BiO)_2CO_3$ clusters onto the

surface of TiO_2, which results in an atomic ratio of Bi/Ti of 0.02, its photocatalytic activity was decreased and its biocompatibility in healthy cells increased, while maintaining its size, morphology, and UV blocking ability. Moreover, the nanocomposites displayed a reduced toxicity in HaCaT cells upon irradiation with simulated sunlight in comparison to TiO_2 NPs, which indicates that the composites are capable of reducing the photo-induced generation of ROS.

ASSOCIATED CONTENT

Supporting Information

The Supporting Information is available free of charge on the ACS Publications website at DOI: xx.

Figures are provided: Adapted light emission profile of the OSRAM Ultra-Vitalux® 300 W Sunlamp; TEM images with high resolution EDS mapping of TiO_2 NPs and $TiO_2/(BiO)_2CO_3$ nanocomposites Bi/Ti 2 and 4 at.%; High resolution XPS spectra of the N 1s, O 1s, and Ti 2p regions; Apparent rate constant curves for the degradation of crystal violet under exposure to UV-visible light and AM 1.5 G one sun (100 mW/cm^2). Table is provided: High resolution XPS of Bi 4f, Ti 2p, and C 1s.

AUTHOR INFORMATION

Corresponding Author

* (K.K.) E-mail: konstan@uow.edu.au

Notes

The authors declare no competing financial interest.

ACKNOWLEDGEMENTS

This work was supported by the Australian Research Council (ARC DP160102627) and the 2017 University of Wollongong Global Challenges Seed Grant "New generation sunscreens optimized for Australian extreme exposure conditions and reliable in vitro test protocols for SPF and critical wavelength". Furthermore, the authors acknowledge the use of the facilities and the assistance of Dr. G. Casillas-Garcia at the Electron Microscopy Centre at the University of Wollongong. We would also like to thank Dr. D. Shi at the University of Wollongong for conducting the XPS measurements and Dr. T. Silver for help with editing the manuscript.

REFERENCES

(1) D'Orazio, J.; Jarrett, S.; Amaro-Ortiz, A.; Scott, T. UV Radiation and the Skin. *Int. J. Mol. Sci.* **2013**, *14*, 12222 – 12248.

(2) Meyskens, F. L.; Farmer, P.; Fruehauf, J. P. Redox Regulation in Human Melanocytes and Melanoma. *Pigment Cell Melanoma Res.* **2001**, *14*, 148 – 154.

(3) Crosera, M.; Bovenzi, M.; Maina, G.; Adami, G.; Zanette, C.; Florio, C.; Larese, F. F. Nanoparticle Dermal Absorption and Toxicity: A Review of the Literature. *Int. Arch. Occup. Environ. Health* **2009**, *82*, 1043 – 1055.

(4) Australian Government, Department of Health, Literature Review on the Safety of Titanium Dioxide and Zinc Oxide Nanoparticles in Sunscreens, https://www.tga.gov.au/sites/default/files/nanoparticles-sunscreens-review-_2016_1.pdf, accessed: January, 2018.

(5) Popov, A. P.; Lademann, J. R.; Priezzhev, A. V.; Myllylä, R. Effect of Size of TiO_2 Nanoparticles Embedded into Stratum Corneum on Ultraviolet-A and Ultraviolet-B Sun-Blocking Properties of the Skin. *J. Biomed. Opt.* **2005**, *10*, 64037 – 64039.

(6) Smijs, T. G.; Pavel, S. Titanium Dioxide and Zinc Oxide Nanoparticles in Sunscreens: Focus on their Safety and Effectiveness. *Nanotechnol. Sci. Appl.* **2011**, *4*, 95 – 112.

(7) Zhang, J.; Nosaka, Y. Mechanism of the OH Radical Generation in Photocatalysis with TiO_2 of Different Crystalline Types. *J. Phys. Chem. C* **2014**, *118*, 10824 – 10832.

(8) Gaspar, L.; Campos, P. M. Rheological Behavior and the SPF of Sunscreens. *Int. J. Pharm.* **2003**, *250*, 35 – 44.

(9) Serpone, N.; Salinaro, A.; Emeline, A. V.; Horikoshi, S.; Hidaka, H.; Zhao, J. An In Vitro *S*ystematic Spectroscopic Examination of the Photostabilities of a Random Set of Commercial Sunscreen Lotions and their Chemical UVB/UVA Active Agents. *Photochem. Photobiol. Sci.* **2002**, *1*, 970 – 981.

(10) Briand, G. G.; Burford, N. Bismuth Compounds and Preparations with Biological or Medicinal Relevance. *Chem. Rev.* **1999**, *99*, 2601 – 2658.

(11) Rodilla, V.; Miles, A. T.; Jenner, W.; Hawksworth, G. M. Exposure of Cultured Human Proximal Tubular Cells to Cadmium, Mercury, Zinc and Bismuth: Toxicity and Metallothionein Induction. *Chem. Biol. Interact.* **1998**, *115*, 71 – 83.

(12) Bradley, M.; Singleton, M.; Po, A. Bismuth Toxicity – A Reassessment. *J. Clin. Pharm. Ther.* **1989**, *14*, 423 – 441.

(13) Tillman, L.; Drake, F.; Dixon, J.; Wood, J. Safety of Bismuth in the Treatment of Gastrointestinal Diseases. *Aliment. Pharmacol. Ther.* **1996**, *10*, 459 – 467.

(14) Iuchi, K.; Hatano, Y.; Yagura, T. Heterocyclic Organobismuth (III) Induces Apoptosis of Human Promyelocytic Leukemic Cells through Activation of

Caspases and Mitochondrial Perturbation. *Biochem. Pharmacol.* **2008**, *76*, 974 – 986.

(15) Smith, K. A.; Deacon, G. B.; Jackson, W. R.; Tiekink, E. R. T.; Rainone, S.; Webster, L. K. Preparation and Anti-Tumour Activity of Some Arylbismuth (III) Oxine Complexes. *Met. Based Drugs* **1998**, *5*, 295 – 304.

(16) Klaveness, J.; Berg, A.; Almen, T.; Golman, K.; Droege, M.; Yu, S. B. Non-Cluster Type Bismuth Compounds. United States Patent, *US 5817289 A*, **1998**.

(17) Drewes, D. A.; Parker, F. T. Flexible, Highly Radiopaque Plastic Material Catheter. United States Patent, *US 5300048*, **1994**.

(18) Chen, R.; So, M. H.; Yang, J.; Deng, F.; Che, C. M.; Sun, H. Fabrication of Bismuth Subcarbonate Nanotube Arrays from Bismuth Citrate. *Chem. Comm.* **2006**, *21*, 2265 – 2267.

(19) Chen, R.; Cheng, G.; So, M. H.; Wu, J.; Lu, Z.; Che, C. M.; Sun, H. Bismuth Subcarbonate Nanoparticles Fabricated by Water-in-Oil Microemulsion-Assisted Hydrothermal Process Exhibit Anti-Helicobacter Pylori Properties. *Mater. Res. Bull.* **2010**, *45*, 654 – 658.

(20) Canonica, S.; Kohn, T.; Mac, M.; Real, F. J.; Wirz, J.; Von Gunten, U. Photosensitizer Method to Determine Rate Constants for the Reaction of Carbonate Radical with Organic Compounds. *Environ. Sci. Technol.* **2005**, *39*, 9182 – 9188.

(21) Tanaka, T.; Tsuzuki, K.; Takagi, T. Chemical Oxidation of Organic Matter in Secondary-Treated Municipal Wastewater by Using Methods Involving Ozone, Ultraviolet Radiation and TiO_2 Catalyst. *Water Sci. Technol.* **2001**, *43*, 295 – 302.

(22) Selvamani, T.; Asiri, A. M.; Al-Youbi, A. O.; Anandan, S. Emergent Synthesis of Bismuth Subcarbonate Nanomaterials with Various Morphologies

towards Photocatalytic Activities – An Overview. *Mater. Sci. Forum* **2013**, *764*, 169 – 193.

(23) Liu, Y.; Wang, Z.; Huang, B.; Yang, K.; Zhang, X.; Qin, X.; Dai, Y. Preparation, Electronic Structure, and Photocatalytic Properties of $Bi_2O_2CO_3$ Nanosheet. *Appl. Surf. Sci.* **2010**, *257*, 172 – 175.

(24) Tang, J.; Cheng, G.; Zhou, H.; Yang, H.; Lu, Z.; Chen, R. Shape-Dependent Photocatalytic Activities of Bismuth Subcarbonate Nanostructures. *J. Nanosci. Nanotechnol.* **2012**, *12*, 4028 – 4034.

(25) Dong, X.; Zhang, W.; Cui, W.; Sun, Y.; Huang, H.; Wu, Z.; Dong, F. Pt Quantum Dots Deposited on N-Doped $(BiO)_2CO_3$: Enhanced Visible Light Photocatalytic NO Removal and Reaction Pathway. *Catal. Sci. Technol.* **2017**, *7*, 1324 – 1332.

(26) Feng, X.; Zhang, W.; Sun, Y.; Huang, H.; Dong, F. Fe(III) Cluster-Grafted $(BiO)_2CO_3$ Superstructures: *In Situ* DRIFTS Investigation on IFCT-Enhanced Visible Light Photocatalytic NO Oxidation. *Environ. Sci. Nano* **2017**, *4*, 604 – 612.

(27) Feng, X.; Zhang, W.; Deng, H.; Ni, Z.; Dong, F.; Zhang, Y. Efficient Visible Light Photocatalytic NO_x Removal with Cationic Ag Clusters-Grafted $(BiO)_2CO_3$ Hierarchical Superstructures. *J. Hazard. Mater.* **2017**, *322*, 223 – 232.

(28) Madhusudan, P.; Ran, J.; Zhang, J.; Yu, J.; Liu, G. Novel Urea Assisted Hydrothermal Synthesis of Hierarchical $BiVO_4/Bi_2O_2CO_3$ Nanocomposites with Enhanced Visible-Light Photocatalytic Activity. *Appl. Catal. B* **2011**, *110*, 286 – 295.

(29) Chen, L.; Yin, S. F.; Luo, S. L.; Huang, R.; Zhang, Q.; Hong, T.; Au, P. C. $Bi_2O_2CO_3$/BiOI Photocatalysts with Heterojunctions Highly Efficient for Visible-

Light Treatment of Dye-Containing Wastewater. *Ind. Eng. Chem. Res.* **2012**, *51*, 6760 – 6768.

(30) Huang, Y.; Wang, W.; Zhang, Q.; Cao, J. J.; Huang, R. J.; Ho, W.; Lee, S. C. In situ Fabrication of α-Bi_2O_3/$(BiO)_2CO_3$ Nanoplate Heterojunctions with Tunable Optical Property and Photocatalytic Activity. *Sci. Rep.* **2016**, *6*, 23435.

(31) Ao, Y.; Xu, L.; Wang, P.; Wang, C.; Hou, J.; Qian, J.; Li, Y. Graphene and TiO_2 Co-Modified Flower-Like $Bi_2O_2CO_3$: A Novel Multi-Heterojunction Photocatalyst with Enhanced Photocatalytic Activity. *Appl. Surf. Sci.* **2015**, *355*, 411 – 418.

(32) Dong, F.; Lee, S.; Wu, Z.; Huang, Y.; Fu, M.; Ho, W. K.; Zou, S.; Wang, B. Rose-Like Monodisperse Bismuth Subcarbonate Hierarchical Hollow Microspheres: One-Pot Template-Free Fabrication and Excellent Visible Light Photocatalytic Activity and Photochemical Stability for NO Removal in Indoor Air. *J. Hazard. Mater.* **2011**, *195*, 346 – 354.

(33) Cheng, H.; Huang, B.; Yang, K.; Wang, Z.; Qin, X.; Zhang, X.; Dai, Y. Facile Template-Free Synthesis of $Bi_2O_2CO_3$ Hierarchical Microflowers and Their Associated Photocatalytic Activity. *ChemPhysChem* **2010**, *11*, 2167 – 2173.

(34) Barker, P. J.; Branch, A. The Interaction of Modern Sunscreen Formulations with Surface Coatings. *Prog. Org. Coat.* **2008**, *62*, 313 – 320.

(35) Australian Government, NMI Nanometrology, XRD Phase Analysis of TiO_2 Sunscreens, https://1bps6437gg8c169i0y1drtgz-wpengine.netdna-ssl.com/wp-content/uploads/2017/legacy/NMI-report-XRD-anatase.pdf, accessed: January, 2018.

(36) Tauc, J. Optical Properties of Amorphous Semiconductors, *Amorphous and Liquid Semiconductors*, Springer, Boston, MA, 1974, 159 – 220.

(37) Senthilkumaar, S.; Porkodi, K. Heterogeneous Photocatalytic Decomposition of Crystal Violet in UV-Illuminated Sol–Gel Derived Nanocrystalline TiO_2 Suspensions. *J. Colloid Interface Sci.* **2005**, *288*, 184 – 189.

(38) Cornish-Bowden, A. *Fundamentals of Enzyme Kinetics*, Weinheim, Germany: Wiley-Blackwell, 2012.

(39) Mosmann, T. Rapid Colorimetric Assay for Cellular Growth and Survival: Application to Proliferation and Cytotoxicity Assays. *J. Immunol. Methods* **1983**, *65*, 55 – 63.

(40) Van Meerloo, J.; Kaspers, G. J.; Cloos, J. Cell Sensitivity Assays: The MTT Assay. *Cancer Cell Culture*. Humana Press, New York, 2011, 237 – 245.

(41) Buonsanti, R.; Grillo, V.; Carlino, E.; Giannini, C.; Gozzo, F.; Garcia-Hernandez, M.; Garcia, M. A.; Cingolani, R.; Cozzoli, P. D. Architectural Control of Seeded-Grown Magnetic−Semiconductor Iron Oxide−TiO_2 Nanorod Heterostructures: The Role of Seeds in Topology Selection. *J. Am. Chem. Soc.* **2010**, *132*, 2437 – 2464.

(42) Cozzoli, P. D.; Pellegrino, T.; Manna, L. Synthesis, Properties and Perspectives of Hybrid Nanocrystal Structures. *Chem. Soc. Rev.* **2006**, *35*, 1195 – 1208.

(43) Hu, H.; Xiao, C. The Effect of Fabrication Conditions on the Morphology and Photocatalytic Activity of Bismutite $Bi_2O_2CO_3$ Particles. *Open J. Phys. Chem.* **2017**, *7*, 1.

(44) Butler, J. N. *Carbon Dioxide Equilibria and Their Applications*. Lewis Publishers, Inc., Chelsea, MI, CRC Press, 1991.

(45) Brune, D.; Novak, J. The Use of Carbonate Equilibrium Chemistry in Quantifying Algal Carbon Uptake Kinetics. *Appl. Microbiol. Biotechnol.* **1981**, *13*, 71 – 76.

(46) Raj, K. J. A.; Viswanathan, B. Effect of Surface Area, Pore Volume and Particle Size of P25 Titania on the Phase Transformation of Anatase to Rutile. *Indian J. Chem. Sect. A* **2009**, *48*, 1378 – 1382.

(47) Dharmadhikari, V. S.; Sainkar, S.; Badrinarayan, S.; Goswami, A. Characterisation of Thin Films of Bismuth Oxide by X-Ray Photoelectron Spectroscopy. *J. Electron. Spectrosc. Relat. Phenom.* **1982**, *25*, 181 – 189.

(48) Lu, B.; Zhu, Y. Synthesis and Photocatalysis Performances of Bismuth Oxynitrate Photocatalysts with Layered Structures. *Phys. Chem. Chem. Phys.* **2014**, *16*, 16509 – 16514.

(49) Houas, A.; Lachheb, H.; Ksibi, M.; Elaloui, E.; Guillard, C.; Herrmann, J. M. Photocatalytic Degradation Pathway of Methylene Blue in Water. *Appl. Catal. B* **2001**, *31*, 145 – 157.

(50) Celardo, I.; De Nicola, M.; Mandoli, C; Pedersen, J. Z.; Traversa, E.; Ghibelli, L. Ce^{3+} Ions Determine Redox-Dependent Anti-Apoptotic Effect of Cerium Oxide Nanoparticles. *ACS Nano* **2011**, *5*, 4537 – 4549.

(51) Esch, F.; Fabris, S.; Zhou, L.; Montini, T.; Africh, C.; Fornasiero, P.; Comelli, G.; Rosei, R. Electron Localization Determines Defect Formation on Ceria Substrates. *Science* **2005**, *309*, 752 – 755.

(52) Masschelein, W. J. *Ultraviolet Light in Water and Wastewater Sanitation*, Lewis Publishers, Boca Raton, Florida, 2002, 59.

(53) Huang, J.; Mabury, S. A. Steady-State Concentrations of Carbonate Radicals in Field Waters. *Environ. Toxicol. Chem.* **2000**, *19*, 2181 – 2188.

(54) Xing, M.; Qui, B.; Du, M.; Zhu, Q.; Wang, L.; Zhang, J. Spatially Separated CdS Shells Exposed with Reduction Surfaces for Enhancing Photocatalytic Hydrogen Evolution. *Adv. Funct. Mater.* **2017**, *27*, 1702624 (1 – 10).

(55) Zhou, Y.; Liu, Y.; Liu, P.; Zhang, W.; Xing, M.; Zhang, J. A Facile Approach to Further Improve the Substitution of Nitrogen into Reduced TiO_{2-x} with an Enhanced Photocatalytic Activity. *Appl. Catal. B* **2015**, *170*, 66 – 73.

(56) Rancan, F.; Nazemi, B.; Rautenberg, S.; Ryll, M.; Hadam, S.; Gao, Q.; Hackbarth, S.; Haag, S.; Graf, C.; Rühl, E. Ultraviolet Radiation and Nanoparticle Induced Intracellular Free Radicals Generation Measured in Human Keratinocytes by Electron Paramagnetic Resonance Spectroscopy. *Skin Res. Technol.* **2014**, *20*, 182 – 193.

(57) Xuan, S.; Wang, F.; Lai, J. M.; Sham, K. W.; Wang, Y. X. J.; Lee, S. F.; Yu, J. C.; Cheng, C. H.; Leung, K. C. F. Synthesis of Biocompatible, Mesoporous Fe_3O_4 Nano/Microspheres with Large Surface Area for Magnetic Resonance Imaging and Therapeutic Applications. *ACS Appl. Mater. Interfaces* **2011**, *3*, 237 – 244.

(58) Mewada, A.; Pandey, S.; Shinde, S.; Mishra, N.; Oza, G.; Thakur, M.; Sharon, M.; Sharon, M. Green Synthesis of Biocompatible Carbon Dots Using Aqueous Extract of Trapa Bispinosa Peel. *Mater. Sci. Eng. C* **2013**, *33*, 2914 – 2917.

(59) Yin, J. J.; Liu, J.; Ehrenshaft, M.; Roberts, J. E.; Fu, P. P.; Mason, R. P.; Zhao, B. Phototoxicity of Nano Titanium Dioxides in HaCaT Keratinocytes – Generation of Reactive Oxygen Species and Cell Damage. *Toxicol. Appl. Pharmacol.* **2012**, *263*, 81 – 88.

(60) Xue, C.; Luo, W.; Yang, X. I. A Mechanism for Nano-Titanium Dioxide-Induced Cytotoxicity in HaCaT Cells under UVA Irradiation. *Biosci. Biotechnol. Biochem.* **2015**, *79*, 1384 – 1390.

(61) Tyagi, N.; Srivastava, S. K.; Arora, S.; Omar, Y.; Mohammad Ijaz, Z. M.; Al-Ghadhban, A.; Deshmukh, S. K.; Carter, J. E.; Singh, A. P.; Singh, S. Comparative Analysis of the Relative Potential of Silver, Zinc-Oxide and Titanium-Dioxide Nanoparticles Against UVB-Induced DNA Damage for the Prevention of Skin Carcinogenesis. *Cancer Lett.* **2016**, *383*, 53 – 61.

(62) Gao, X.; Wang, Y.; Peng, S.; Yue, B.; Fan, C.; Chen, W.; Li, X. Comparative Toxicities of Bismuth Oxybromide and Titanium Dioxide Exposure on Human Skin Keratinocyte Cells. *Chemosphere* **2015**, *135*, 83 – 93.

Table of Contents